ACS APPLIED MATERIALS & INTERFACES

www.acsami.org

Research Article

Transparent and Robust Superhydrophobic Structure on Silica Glass Processed with Microstereolithography Printing

Han Zhang, Yu-Qing Liu, Shaoqing Zhao, Long Huang, Zhi Wang,* Zhiyong Gao, Zhiwei Zhu,* Dahai Hu, and Hua Liu*

Cite This: *ACS Appl. Mater. Interfaces* 2023, 15, 38132−38142

Read Online

ACCESS | Metrics & More | Article Recommendations | Supporting Information

ABSTRACT: Silica glass devices are widely used due to their exceptional physical and chemical properties. However, prolonged usage may result in abrasion and contamination of silica glass devices, adversely affecting the service life. One of the most effective solutions to this issue is surface modification, in which superhydrophobicity with high transmittance and mechanical robustness is highly desired. Inspired by the concept of protective armor, we proposed a novel approach for the direct integration of robust and transparent superhydrophobic structures on silica glass. In this method, micro-stereolithography synergistic heat treatment processes are used to create a micrometer-scale biomimetic frame on the surface of silica glass and then filled with in situ deposited nanoparticles. The superhydrophobicity of the surface can be obtained through the nanoparticles, and the biomimetic frame can protect the surface from direct contact with external objects to achieve durability. This process allows the preparation of superhydrophobic silica structures on the silica device surface at temperatures below its melting point, which prevents any damage to the devices during the heat treatment. Moreover, up to 90% transmittance does not affect the performance of silica devices. The composite structure maintains a contact angle of over 150° after multiple abrasion tests, verifying the mechanical robustness. This innovative process paves the way for forming a high mechanical robustness and excellent transmittance protective layer on silica glass devices, which expands the application field.

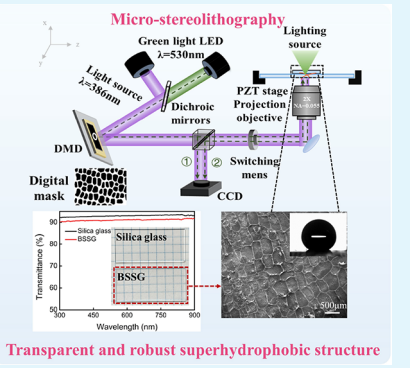

KEYWORDS: *microstereolithography, silica glass, superhydrophobic structures, high transmittance, mechanical robustness*

1. INTRODUCTION

Silica glass has attracted significant attention in optics because of its splendid optical transmittance, broadly applicable spectrum, high environmental suitability, and high laser damage threshold.[1−7] Optical devices based on silica glass often exhibit excellent physicochemical properties and optical performance. In recent years, the rapid development of additive manufacturing technology has provided an effective processing method for the preparation of silica glass devices.[8−12] As a result, numerous difficult-to-machine glass devices such as lenses, microlens arrays, and microfluidic channels have been extensively researched and fabricated.[8,13−17] However, long-term practical applications may cause abrasion and contamination on the surfaces of silica glass devices in contact with air due to their hydrophilicity. For example, long-term exposure of the optical lens device can result in abrasion and the accumulation of large amounts of contaminants. Moreover, high air humidity could cause fogging and corrosion on the surface of silica devices, leading to decreased transparency and surface damage.[18−21] These damages have a severe impact on the life of the device. Manual cleaning is often adopted to minimize the harmful effects of surface contamination and maintain surface cleanliness. Still, this method undoubtedly increases labor costs and the probability of defects such as scratches. Therefore, self-cleaning is particularly important in order to ensure high transmittance and abrasion resistance and prolong the service life of silica glass devices.

Self-cleaning often relies on superhydrophobicity, which reduces the water adhesion on the device surface and enables the rapid slide of water droplets. This sliding motion effectively removes contaminants, ensuring a consistently clean surface and maintaining high optical transmittance of the device.[22−24] Inspired by the "lotus effect", the preparation of superhydrophobic surfaces is based on two primary considerations: reducing the surface free energy and increasing the roughness.[25−27] Currently, various methods such as laser processing,[28−32] templating method,[33] sol−gel method,[34,35] and chemical vapor deposition[36,37] have been adopted to achieve

Received: June 6, 2023
Accepted: July 18, 2023
Published: July 28, 2023

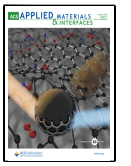

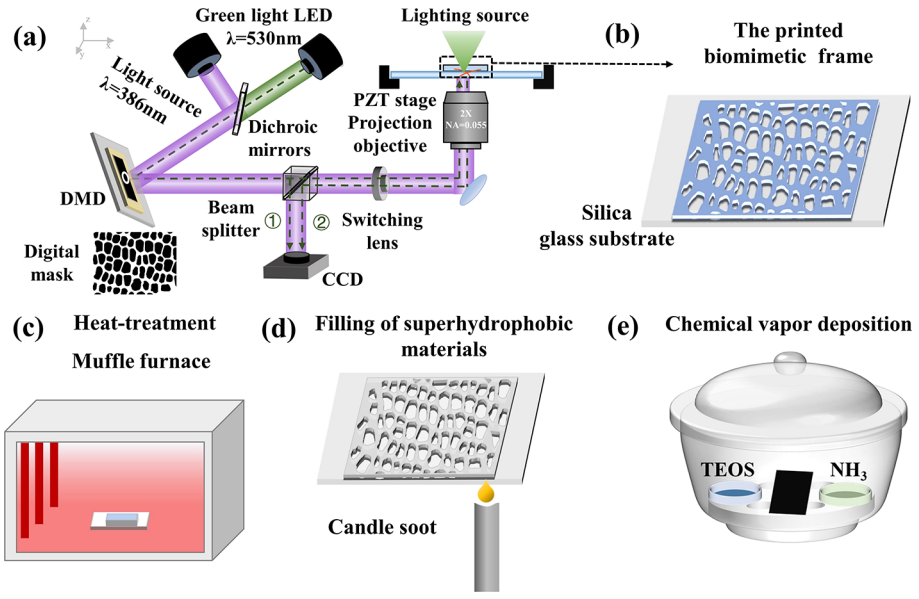

Figure 1. Fabrication processes for transparent and robust superhydrophobic structure on silica glass. Panels (a) and (b) illustrate the composition of the DMD-μSLA system and the structure printed by this system. Panel (c) shows the heat-treatment process. Panels (d) and (e) present the process of the in situ deposition method.

superhydrophobicity. Considering that the fabrication of microstructures on the surface of optical devices may seriously affect the performance of the device, the methods to achieve superhydrophobicity on the surface of silica glass mostly rely on spraying hydrophobic coatings.[38−40] However, the superhydrophobic coatings are not mechanically stable, which are easily detached from the glass surface and can hardly resist mechanical abrasion. Achieving hydrophobicity, transparency, and mechanical robustness simultaneously on silica glass device surfaces is still challenging. Recently, the concept of protective armor has been proposed to achieve wettability and mechanical robustness through two different scale structures. This method can effectively solve the above problems, but meanwhile, it imposes strict requirements on the processing technology.[41]

In this work, a novel solution for the direct integration of robust and transparent superhydrophobic coating on silica glass has been presented. The process utilizes a self-built digital micromirror device microstereolithography (DMD μ-SLA) system and "liquid glass" materials. A silica biomimetic frame structure containing nanoparticles has been successfully prepared on the silica glass surface via the μ-SLA and in situ deposition technology. The structure mimicked in this work is the surface of allium seeds. Regarding the seeds, detailed scanning electron microscope (SEM) and dynamic, static contact angle test results are shown in Figures S1 and S2, respectively. The test results are described in detail in the Supporting Information. However, in this work, we have chosen to mimic only the closely arranged ring-like structure of the allium seed surfaces. The unique structure facilitates the accommodation of more superhydrophobic nanoparticles, while the irregularity and complexity of the structure confirm the fabrication flexibility of the proposed manufacturing process. The nanoparticles endow the glass surface with superhydrophobicity, while the frame can protect the surface structures from direct contact with the external. Wettability, transmittance, and mechanical robustness tests have shown that the structures exhibit excellent hydrophobicity, optical transmittance, and robust properties. The composite structure remains superhydrophobic even after being subjected to high temperatures, acid and alkali solvent immersion, water flow, and mechanical abrasion. Additionally, the innovative revelation and verification of the shrinkage type during the heat treatment of synergistic glass substrates provide guidance for subsequent structural compensation. The μ-SLA system, with ultrahigh processing accuracy, can rapidly prepare any desired structure on the surface of silica glass. Our proposed fabrication method provides the technical basis for achieving self-cleaning and abrasion-resistance silica glass devices to meet specific application requirements.

2. RESULTS AND DISCUSSION

To complete the fabrication efficiently, the DMD μ-SLA system was set up as shown in Figure 1a. The DMD μ-SLA system consists of a front-end illumination system, a digital micromirror device, a projection lens system, a piezoelectric moving platform, and a mechanical and electrical control system. The front-end illumination system employs a LED light source with a central wavelength of 386 nm to shine on DMD. The DMD chip contains 1024 × 768 micromirrors that tune the light pattern according to the input mask. In addition, a 2× objective lens (NA = 0.055) is used as a projection lens to reduce the size. Each micromirror measures 13.68 × 13.68 μm in this system, representing a single pixel. After the 2× lens reduction, the single pixel size is 6.84 μm theoretically, and the maximum machining size is 7004.16 × 5352.12 μm. DMD loads the mask pattern to be exposed, and the reduced pattern is projected onto a glass substrate with "liquid glass". Then, "liquid glass" is underexposed until a complete object is formed. The fabrication process of the biomimetic frame is described in Figure 1a−c. Furthermore, the fabrication processes of the superhydrophobic nanoparticles for frame-filling are illustrated in Figure 1d,e. For more details, refer to the Experimental Section.

In order to validate the proposed approach, an experimental verification was conducted on the surface of silica glass. To

https://doi.org/10.1021/acsami.3c08125
ACS Appl. Mater. Interfaces 2023, 15, 38132−38142

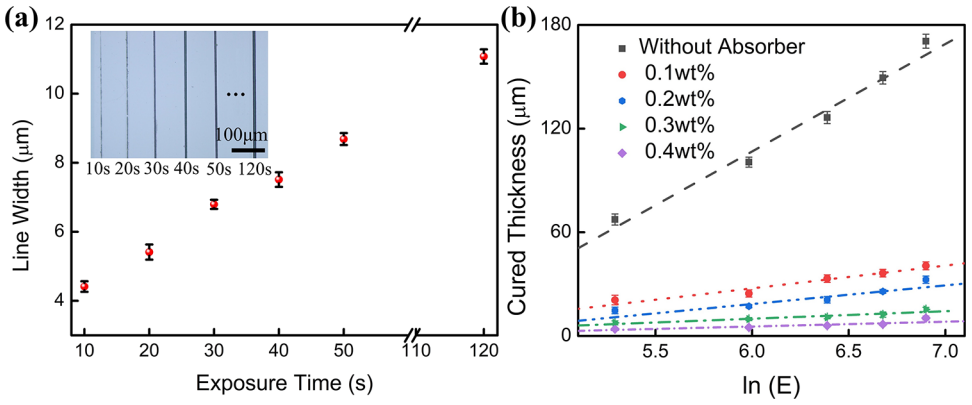

Figure 2. (a) Exposure time versus line width of a single line in a μ-SLA system, inset shows a microscopic image of a single pixel line with different exposure times; (b) variation of the cured thickness versus exposure of "liquid glass".

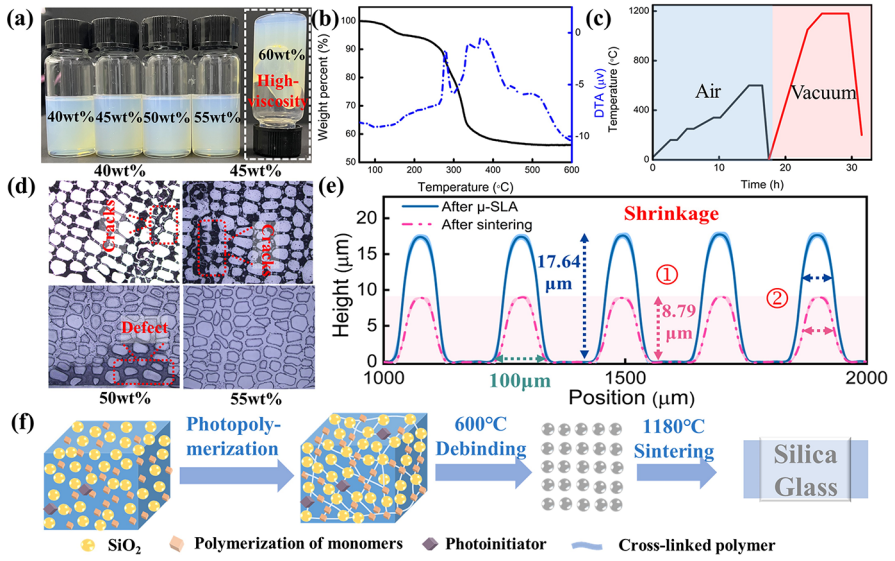

Figure 3. (a) Photographs of "liquid glass" with different silica contents. TG-DTA curves (b) and heating rates (c) for "liquid glass". Panel (d) compares the results obtained after sintering of "liquid glass" with varying silica contents. Panel (e) illustrates the profile testing results of the microstructure before and after heat treatment. Panel (f) shows the shrinkage mechanism.

enhance hydrophobic properties, two important factors need to be focused on: narrow enough edges and customized frame height to accommodate more silica particles, which requires a defined horizontal and vertical resolution for μ-SLA. Thus, the effect of exposure time on the single pixel line width of the configured "liquid glass" was investigated. Figure 2a shows the line width versus exposure time, which increases with increasing exposure time from a minimum of 4.47 to 11.31 μm. The inset of Figure 2a displays a microscopic image of a single line captured at various exposure times from 10 to 50 and 120 s. As seen in the inset, the lines appear broken at exposure times of 10 and 20 s due to underexposure. The line width is close to the unit pixel size (6.84 μm) at an exposure time of 30s. Also, when the exposure time exceeds 30 s, all are in the overexposed states. However, the overexposed state may be conducive to fabricating superhydrophobic surfaces. See Figure 5 for more reasons. The main reasons are explained in the related description of Figure 5.

The height of the structure is a crucial factor in achieving superhydrophobicity and high robustness. Therefore, it is particularly important to investigate the relationship between exposure dose and exposure thickness. In order to improve the vertical resolution of "liquid glass", a suitable amount of UV absorber was added. For μ-SLA, the processing thickness is proportional to the exposure time. Figure 2b shows the C_d–ln(E) relationship between exposure volume and thickness. With the addition of the absorber, the vertical resolution of the "liquid glass" gradually increases. A vertical resolution of 5 μm is achieved at 0.4 wt % of the Sudan orange G. Based on the empirical equation for photopolymerization additive manufacturing (1), the required exposure time based on the expected exposure thickness can be calculated[42]

$$C_d = D_p \ln\left(\frac{E}{E_c}\right) \tag{1}$$

where C_d is the curing depth, D_p is the penetration depth indicated by the slope of the curve, E_c is the critical exposure dose expressed by the x-intercept of the curve, and E is the energy dose, which is the product of the optical power density and the exposure time. All the cured texts of "liquid glass" are measured under an optical power density of 19.84 mW/cm^2. Based on the calculations, the exposure is performed on a silica glass substrate to obtain a biomimetic microstructure (green body). To further confirm whether the thickness is uniform, a

https://doi.org/10.1021/acsami.3c08125
ACS Appl. Mater. Interfaces 2023, 15, 38132−38142

profile test on the exposed structure is performed. Also, the test results are shown in Figure S3. Both the inset and the profile curves confirm the uniformity of the structure after solidification.

The obtained green body has micrometer-sized frames, which have poor mechanical properties and are often accompanied by cracking during fabrication. In addition, as the green body needs to be heat-treated to become silica glass, cracks in the microstructure often occur at both the development and heat-treatment stages. Cracking during development is often caused by the extremely fast volatilization of the organic solvent used to clean the unpolymerized "liquid glass", leading to uneven stresses within the printed object. This can be removed by using a slower evaporating solvent, such as 5‰ NaOH solution. The occurrence of cracking during the heat treatment stage is often due to a mismatch in the heating rate and the silica content of "liquid glass".

Photographs of "liquid glass" with different silica contents are shown in Figure 3a to investigate the factors that lead to cracking during heat treatment. These samples will be used for microstructure fabrication. It should be noted that when the content of SiO_2 is up to 60 wt %, the "liquid glass" becomes less fluid and more viscous, making the μ-SLA process impossible. Therefore, the materials that can be used for μ-SLA are "liquid glass" with a SiO_2 content of 40−55 wt %.

The heat treatment process is often very time-consuming and can lead to several defects, including cracking, delamination, distortion, and collapse, which ultimately impact the integrity of the sample. However, the heating rate during the heat treatment can be optimized by the TG-DTA curve, as demonstrated in Figure 3b. TG analysis reveals four distinct stages of mass loss during the process of debinding. According to the test results, it can be inferred that the 4.41% mass loss between 60 and 160 °C is primarily attributed to the evaporation of water. The mass loss of 3.65% occurs between 160 and 250 °C owing to the evaporation of unpolymerized resin. On the other hand, at a higher temperature ranging from 250 to 340 °C, 29.53% of the mass loss is primarily caused by the oxidative decomposition of the polymer. Subsequently, from 340 to 600 °C, the removal of incompletely oxidized carbonyl groups from the printed parts accounts for 6.81% of the mass loss.[3,43,44] Moreover, the remaining mass accounts for 55.6%, which is close to the SiO_2 content of 55 wt %. To ensure the integrity and morphology of the sample, separate holding steps were set for the debinding process at 160, 250, 340, and 600 °C. Additionally, the heating rate was set as 0.5 °C/min from 250 to 340 °C and 1 °C/min for the rest. To ensure uniform heating and prevent distortion of the sample, the heating rate was carefully controlled. Specifically, the rate was set to 3 °C/min from room temperature up to 1050 °C, at which point it was decreased to 1 °C/min until reaching a final temperature of 1180 °C. During the sintering process, the holding time was set as 4 h and subsequently cooled to room temperature within the furnace. The entire heat treatment time was 31.5 h, and the heating rate curve of the entire heat treatment can be seen in Figure 3c.

According to the optimized heat treatment process, silica glass biomimetic structures with different solids contents were prepared (Figure 3d). A vacuum degree of 5×10^{-2} mbar leads to the closure of pores during the heat treatment. The "liquid glass" with a silica content of 40−50 wt % has a lower solid loading which intensifies the volume shrinkage during the sintering process, thus leading to fractures of the structure. In comparison, the "liquid glass" with a solid content of 55 wt % exhibits no cracks or porosity and excellent transparency after vacuum sintering. This suggests that a silica content of 55 wt % is suitable for μ-SLA.

The removal of organic matter and the increasing densification of the samples during the heat treatment process results in a dramatic shrinkage.[3] However, as the μ-SLA is carried out on a silica glass substrate and the heat treatment process is also sintered together with the substrate, the type of shrinkage differs from the conventional linear shrinkage. In consideration of the irregularity of the prepared biomimetic frame, it is difficult to test the same position before and after sintering, resulting in significant measurement errors. We designed regular microstructures using the same material and fabrication technique. Moreover, the Alpha-Step D300 profiler was taken to profile the prepared microstructures. The results of the tests before and after sintering are shown in Figure 3e. The type of shrinkage can be analyzed by comparing the data in Figure 3e. The height of the microstructure before heat treatment is 17.64 μm, and the width in the cycle is 100 μm. After sintering, the width remains the same, the height is reduced to 8.79 μm, and the shrinkage of the Z-direction can be calculated as 49.83%.

If the printed structure undergoes linear shrinkage during the heat treatment, the shrinkage can be calculated by the following formulas 2 and 3:[44]

$$Y_S = 1 - (\varphi)^{1/3} \tag{2}$$

$$\varphi = \frac{w/\rho_g}{w/\rho_g + (1-w)/\rho_p} \tag{3}$$

where Y_S represents the shrinkage rate and w is the content of SiO_2 in the mixed solution; the density of the fused silica glass is denoted as ρ_g, taken as $\rho_g = 2.219$ g/cm^3; the density of the liquid mixture excluding silica, represented as ρ_p, was measured to be 1.125 g/cm^3.

The formula was defined using the ratio of change in volume. Thus, the exponent of 1/3 in formula 2 represents isotropic contraction in the three-dimensional direction (X, Y, and Z directions). Also, if the shrinkage occurs in the one-dimensional direction (Z direction) only, the exponent should be 1.

Unlike isotropic shrinkage, the heat treatment of the biomimetic frame is carried out together with the silica glass substrate, which results in anisotropic shrinkage. The debinding and sintering of the "liquid glass" is essentially the removal of the organic material and the fusion of silica nanoparticles at high temperature and pressure, and the process is described in Figure 3f. Because the heat treatment is carried out together with the silica substrate, the silica substrate undergoes a certain extent of softening at high temperature and pressure, and the silica nanoparticles in the "liquid glass" fuse with the softened substrate. During the heat treatment, the two parts gradually fuse, and the mechanical pull provided by the silica substrate prevents shrinkage of the structure in the X and Y directions. In contrast, there is no mechanical pull in the Z direction, so the biomimetic structure shrinks more in the Z direction after sintering. But if the shrinkage occurs only in one-dimensional (Z direction), the shrinkage rate can be calculated as 61.75%, quite different from the test result of 49.83%.

https://doi.org/10.1021/acsami.3c08125
ACS Appl. Mater. Interfaces 2023, 15, 38132−38142

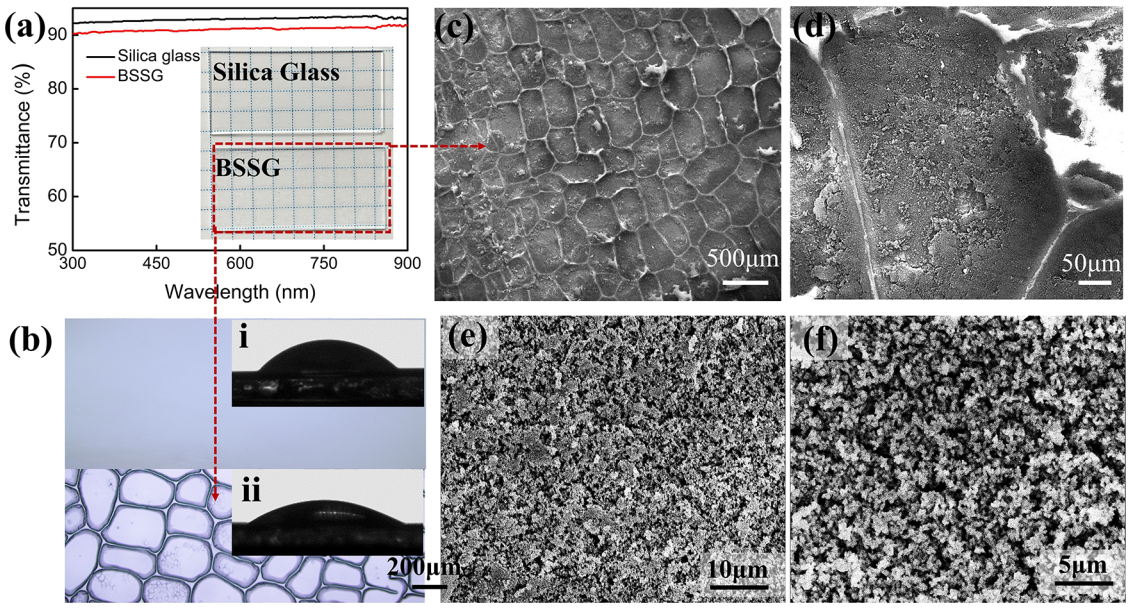

Figure 4. Panel (a) illustrates a picture of the fabricated BSSG and the transmittance spectra. The inset presents a comparison between the transmittance of silica glass and that of BSSG. Panel (b) shows an optical microscope photograph of the BSSG, and insets (i, ii) present the wettability of the silica glass surface with and without the biomimetic frame. Panels (c–f) present SEM images of the BSSG and the internal filler at varying magnifications.

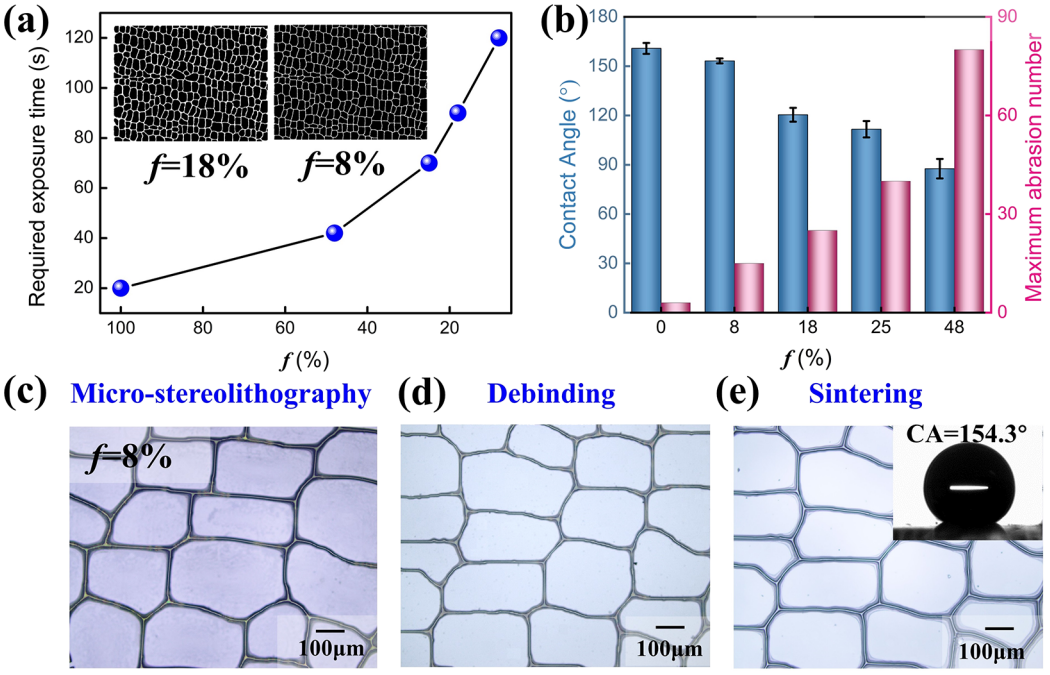

Figure 5. Panel (a) presents the exposure time required for different f to reach the same height of 12 μm. Insets: mask patterns under the condition of f = 18% and f = 8%. Panel (b) shows the effect of f on wettability and mechanical robustness. Panels (c–e) present the photographs after μ-SLA, debinding, and sintering at f = 8%, respectively. The insets show the contact angle after filling with nanoparticles.

The large discrepancy between the theoretical and calculated values suggests that shrinkage does not only occur in the one-dimensional direction. The mechanical pull prevents shrinkage in the X-Y directions of the part in contact with the glass substrate, as evidenced by the consistent widths of the cycle before and after heat treatment. There is shrinkage in the part that is not in contact with the glass substrate, and this shrinkage is reflected in two main points: a reduction in height and a decrease in width, as illustrated in Figure 3e ① and ②. Both of these shrinkages are due to the lack of mechanical pull provided by the substrate in the areas not in contact with the glass substrate. Due to the high height of the printed structure, a greater range of shrinkage can be allowed, and therefore, a greater amount of shrinkage is more likely to occur in the Z direction, while there is also a slight shrinkage in the X and Y directions. In summary, the shrinkage in the Z direction was considered as a shrinkage of 1.5 dimensional, and the exponential of formula 2 should be 2/3. The shrinkage Y_S can be calculated as 47.30%, consistent with the test result of 49.83%.

https://doi.org/10.1021/acsami.3c08125
ACS Appl. Mater. Interfaces 2023, 15, 38132–38142

Figure 4a shows the images of a biomimetic superhydrophobic surface based on silica-glass (BSSG) and silica glass. Furthermore, a comparison of the transmittance between the two samples is also presented. As shown, the transmittance of the manufactured BSSG is lower than the 93% transmittance of silica glass. However, the transmittance in the visible range is still over 90%, rendering it suitable for a diverse range of applications. Figure 4b displays microscope photographs of the silica glass and BSSG. Furthermore, the structural integrity and surface smoothness of BSSG can be confirmed. The inset in Figure 4b shows the CA (38°) of silica glass (i) and the CA (27°) after the growth of the biomimetic structure (ii). The reduction of CA can be attributed to the increased surface roughness resulting from the production of microstructures. In order to present the morphology of the biomimetic structure and the filled particles better, SEM tests were performed. Figure 4c−f shows the SEM images of the BSSG filled with silica nanoparticles at different magnifications. The surface structure and the filled silica nanoparticles of BSSG can be observed. The frame structure of the BSSG is filled with a large number of silica nanoparticles, which is an important guarantee for achieving superhydrophobicity. The composite structure of protective armor synergistic of nanoparticles ensures that even under extreme test conditions such as mechanical abrasion, there is sufficient nanoparticle filling to achieve excellent wettability properties. SEM tests show that the biomimetic frames used to accommodate the superhydrophobic nanoparticles are compact and have a high degree of integrity. Also, the surface morphology of the superhydrophobic nanoparticles used to fill the frame is highly consistent with structures prepared by in situ deposition reported before. [41,45]

Furthermore, the principle of introducing the protective frame is that the introduction of the microstructure must not impact the superhydrophobic properties of the surface.[41] Since the hydrophilicity of silica glass, the width of the protective frame will have a decisive influence on the wettability of the microstructure. The structural occupation f determines the width of the protective frame, and f is defined as the percentage of the white part in the entire mask pattern, as demonstrated in the insets of Figure 5a.

Mechanical robustness and wettability often exist in contradiction. To investigate the impact of structures with various f values on the wettability as well as mechanical properties and to probe for the most suitable f, structures with different f values were fabricated and filled with nanoparticles. When investigating the effect of f on wettability and mechanical properties, it is necessary to ensure that structures with different f values have the same height. As f represents the duty cycle of the white pattern, less duty cycle requires more exposure time during the μ-SLA process. This means that structures with small f values require longer exposure times to achieve the same thickness. For BSSG, the most important feature is the high transmittance and mechanical robustness. If the frame structures of BSSG are too high, too many nanoparticles will be filled, and the high transmittance will be affected. If the structure is too low, the mechanical robustness will be poor. After experimental exploration, we finally settled on a sintered thickness of 6 μm as the optimum thickness. According to the theoretical analysis in Figure 3e, the actual height after exposure is almost 12 μm. Thus, the thickness of the frame could be determined.

Figure 5a illustrates the time required to reach a thickness of 12 μm for structures with f values of 8, 18, 25, 48, and 100%. Although the long exposure time will increase the line width, the overexposure state is rather favorable for fabricating the biomimetic frame structure in the actual processing. This is because the light field intensity of the pixels projected by the DMD exhibits a Gaussian distribution, and because of this, the frame structure will take on a narrow top and wide bottom shape under long-time exposure. The width of the uppermost structure will even present a subpixel size. The narrower the line width, the more beneficial it is to eliminate the influence of the silica with hydrophilic on the entire superhydrophobic surface performance. Therefore, the selection of 120 s exposure time is reasonable.

Figure 5b demonstrates the impact of f on both the wettability and mechanical robustness. The mechanical abrasion test was carried out with a 5 N weight, which was reciprocated over the structure for one cycle as a count. As depicted in Figure 5b, the composite structure exhibits optimal wettability with a CA of 160.8° ± 3.3° when the value of f is set to 0. However, due to the lack of protection from the biomimetic frame, it can only withstand 3 counts of abrasion and is not of high application value. The sample with f = 8% has a CA of 153.4° ± 1.2°, which is close to that of the sample at f = 0 and has superhydrophobic properties. Thanks to the protection of the frame, the structure still has a CA of 151.7° ± 2.0° after 20 abrasions. The abrasion resistance makes this sample very valuable for applications. With the increase of f, the abrasion resistance of the composite structure gradually improves, but the CA continues to decrease. By the time of f = 18%, the contact angle has reduced to around 120.3° ± 2.4°, and the superhydrophobicity is lost. When f increases to 48%, the composite structure can resist 80 mechanical abrasions, but the CA is almost 88.3° ± 2.5°. At this point, hydrophobic properties and the application value are both lost. Therefore, considering both the wettability and the mechanical robustness, f = 8% was considered the optimum percentage. Structures with f = 8% were selected for further testing.

Figure 5c−e shows photographs after μ-SLA, debinding, and sintering at the sample with f = 8%. The debinding process is one of the most time-consuming stages of heat treatment; unwilling deformations, such as cracking, curling, etc., could occur during this process. When unwilling deformation occurs, the preparation of the biomimetic frame could fail. As can be seen from the graphs, no unwanted deformations occur after a reasonable thermal debinding process, which demonstrates the reasonableness of the heating rate based on the TG curve. After high-temperature sintering, BSSG with f = 8% was successfully prepared.

However, the images obtained through the SEM show that the porous structure is heterogeneous (Figure 4c−f). To make the testing of contact angles more reliable, several positions were selected for contact angle testing. The test results are shown in Figure S4; it can be seen that contact angles at different locations of the BSSG are all greater than 150°and with good superhydrophobicity.

In order to define the BSSG surface precisely and to further analyze the adhesion of the BSSG surface to water droplets, dynamic contact angle tests are performed. The test results are shown in Figure S5. The advancing contact angle (θ_A) and receding contact angle (θ_R) of the BSSG were tested to be 156.4° ± 1.2° and 151.5° ± 1.1°, respectively, and the contact angle hysteresis (CAH) is 4.9° ± 2.3°, which means that water droplets may tend to move more easily on the BSSG. Furthermore, the sliding angle (SA) was recorded as 6.8° ±

https://doi.org/10.1021/acsami.3c08125
ACS Appl. Mater. Interfaces 2023, 15, 38132−38142

0.7°. Excellent static and dynamic contact angles confirm the excellent superhydrophobicity of the BSSG. Hence, BSSG can be defined as a superhydrophobic surface.

Dynamic and static contact angle tests and performance comparisons show that the fabricated BSSG samples have excellent superhydrophobic properties, which is compatible with previous works (Table S1).

In summary, the sample with f = 8% has the best wettability and was therefore selected for further testing.

Self-cleaning properties are a distinct characteristic of superhydrophobic surfaces. In order to investigate the self-cleaning capability of BSSG, the soil was separately distributed on both the BSSG and silica glass surfaces, as demonstrated in Figure 6a. Using a pipette, an equal amount of water droplets

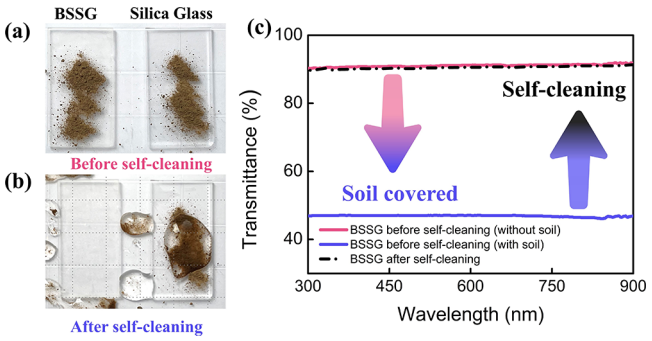

Figure 6. Comparison of the results before (a) and after (b) self-cleaning. Panel (c) presents the transmission spectra of the BSSG in a variety of states.

continuously dropped onto both surfaces. Due to the superhydrophobicity of the BSSG, the droplets roll off the superhydrophobic surface and carry the contaminants away from the surface, leaving a clean BSSG surface. In contrast, owing to the hydrophilicity of the silica glass, the contaminants continue to be present on the silica glass surface, as depicted in Figure 6b. Figure 6c illustrates the transmission spectra of the BSSG in a variety of states. The soil cover reduces the BSSG transmission rate from 90 to 47%. After self-cleaning, the contaminants are completely removed, and the transmission rate increases to 90% again. The entire self-cleaning process can be seen in Movie S1. The above tests show that the BSSG has excellent self-cleaning properties and is of high practical application.

Liquids of various compositions and viscosities were dripped onto the surface of BSSG to test the wettability. As demonstrated in Figure 7a, droplets are spherically distributed on the surface of BSSG, indicating that BSSG exhibits excellent wettability. The volume of liquid used in Figure 7a was approximately 60 μL.

The practical application of BSSG requires thermal stability under high temperatures. A thermostatically heating stage was taken to test the thermal stability of BSSG. The samples were periodically removed, and the contact angle (CA) was measured after cooling to room temperature. The test results are illustrated in Figure 7b, which shows that the CA of the BSSG remains at 152° even after 3 h of exposure to temperatures close to 200 °C. This results from the combination of the silica glass's extremely high thermal stability and the filler material's thermal stability with an upper limit of 350 °C.

Moreover, the practical application of BSSG requires it to be chemically stable in corrosive aqueous media. To assess this, the impact of pH on the surface wettability of BSSG was studied, as can be seen in Figure 7c. The results suggest that the surface of BSSG is not significantly affected by corrosive aqueous media as the CA of water remains nearly 150° at all pH values.

Furthermore, abrasion resistance tests were carried out to explore the mechanical robustness of the structure. The abrasion resistance tests proceeded with a weight of 5 N (Figure 7d). In order to demonstrate the mechanical robustness of the BSSG better, 50 times abrasion tests were carried out. The test results are shown in Figure 7d. As can be seen from the figure, the CA of the BSSG surface is still >150° and with good superhydrophobicity even after 20 times abrasion with a 500 g weight. Continuously increasing the number of abrasions, the CAs present a decreasing trend. The decrease in CA is due to the structural damage of the BSSG surface and the disappearance of the superhydrophobic particles caused by the multiple abrasions. When the abrasions number reaches 50 times, the surface of the BSSG illustrates obvious abrasion, and the frame structure is even fractured to a large extent. The fracture of the structure directly leads to the loss of the superhydrophobic nanoparticles, and the fractured structure also has a negative effect on the CA. After extensive abrasion, the CA of the BSSG decreases significantly. However, even after 50 abrasions, the CA of the BSSG was still 120.1° ± 2.1°, showing a certain degree of hydrophobic properties. This demonstrates the excellent abrasion resistance of the BSSG.

In practical applications, avoiding the influence of water flow on BSSG is unrealistic. Hence, it is crucial to study the effect of water flows on BSSG. The BSSG was subjected to under 20 cm of water with a water velocity of 20 cm/s. Obviously, the contact angle of the BSSG did not change significantly, even after 10 min of water impact (Figure 7e). The microstructure diagrams of the test surface before and after various tests are illustrated in Figure S6.

The mechanism of the BSSG that enables excellent robustness and superhydrophobicity is depicted in Figure 7f. The silica glass frame with ultrahigh mechanical properties provides primary protection to the filling when the surface is worn with mechanical forces, keeping the superhydrophobic filling from being abraded. Continuing to increase the mechanical pressure or abrasion time will lead to the abrasion of the silica glass protective frame and, consequently, to the removal of the superhydrophobic filler. However, due to the thickness of the silica glass protective frame and the superhydrophobic filler, the substructure can still function and achieve superhydrophobicity after damage to the upper structure. Similarly, in water flow experiments, the rigid microscale interconnected frame structure reduces the abrasive effect of high-speed water flow. As a result, the hydrophobic nanomaterials inside the frame were protected. The air trapped inside the enclosed cavity increases the pressure difference between liquid and air, preventing puncture by water flow.[41,46,47] Thus, the superhydrophobicity is maintained.

The feasibility of the proposed fabrication method is demonstrated by these test results under extreme conditions. It is noteworthy that the proposed machining scheme can achieve high transmittance, high robustness, and superhydrophobicity on silica glass substrates simultaneously also means that the process can be applied to the secondary processing of silica glass device surfaces. The modified surface

https://doi.org/10.1021/acsami.3c08125
ACS Appl. Mater. Interfaces 2023, 15, 38132−38142

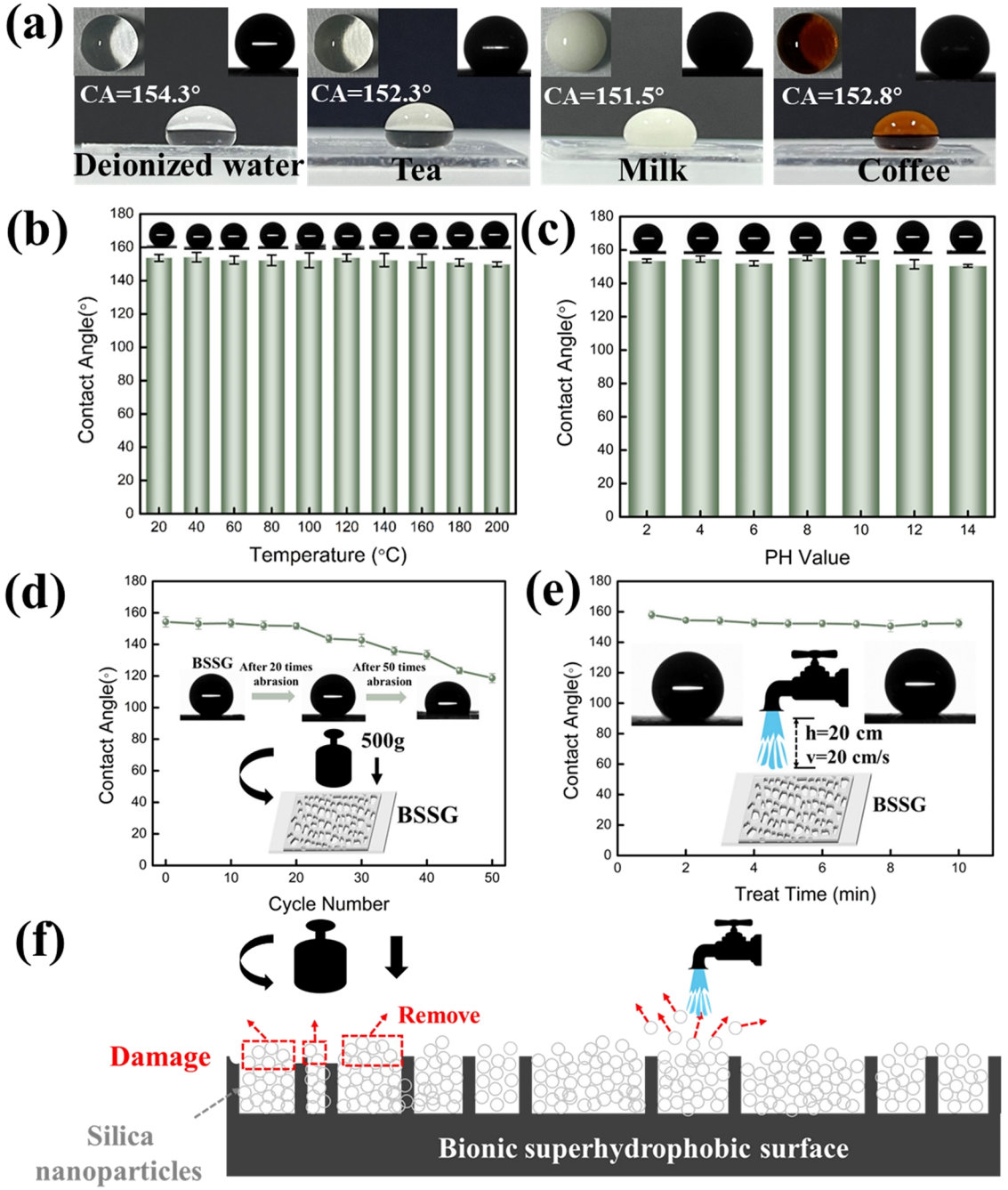

Figure 7. (a) Various fluids were used to test the wettability of BSSG. Panels (b–e) demonstrate the effects of temperature, pH, mechanical abrasion, and water flow on the CA of the BSSG, respectively. The corrosion resistance of the sample was tested after 2 h of exposure to each pH solution. Similarly, the high-temperature resistance of the samples was tested after 3 h of exposure to each temperature value. Panel (f) illustrates the mechanism for excellent robustness and superhydrophobicity is revealed.

of the silica glass device will be more widely used as it will have good robustness without compromising the performance itself.

3. CONCLUSIONS

In this work, an innovative strategy was proposed to directly integrate robust and transparent superhydrophobic structures on silica glass. This strategy allows the modification on the surface of silica glass devices, which retains its properties while providing self-cleaning capabilities and mechanical robustness. The additional excellent properties extend the application and enhance the lifetime of the silica glass devices. In this process, the shrinkage mechanism in the glass phase transformation process and the type of shrinkage are innovatively revealed. The superhydrophobic surfaces produced have an ultrahigh optical transmittance (more than 90%). Contact angle tests at high temperatures, immersion in solutions of different pH values, mechanical abrasion, and after-water droplet impact show the stability of the prepared composite structure. The excellent optical properties and robustness validate the success of the proposed fabrication strategy. This breaks the dilemma of the contradiction between superhydrophobicity and robustness and has opened up new possibilities for the rapid development of optical device machining and applications. Meanwhile, the high processing accuracy of the μ-SLA process

https://doi.org/10.1021/acsami.3c08125
ACS Appl. Mater. Interfaces 2023, 15, 38132−38142

allows the fast and cost-effective preparation of arbitrary microstructures in less than tens of seconds. In addition, the fabrication of highly geometrically complex 3D patterns on glass devices can also be achieved. The method can be widely applied to the protection of arbitrary functional devices such as microlenses, microlens arrays, and even microfluidic chips. Most importantly, the process can also break the material limitation and rapidly prepare arbitrary 3D patterns with complex geometry on the surface of heat-resistant materials such as glass and ceramics. This beneficial and harmless secondary processing method is very promising in terms of material surface modification and material performance enhancement.

4. EXPERIMENTAL SECTION

4.1. Materials. Hydroxyethyl methacrylate (HEMA), Sudan Orange G, phenylbis(2,4,6-trimethylbenzoyl) phosphine oxide (Irgacure 819), tetra(ethylene glycol) diacrylate (TEGDA), diethyleneglycol dibenzoate (DEDB), tetraethoxysilane (TEOS) and trichloro(1*H*,1*H*,2*H*,2*H*-tridecafluoro-*n*-octyl)silane (FOTS) were supplied by Aladdin (China). The silica nanoparticles adopted in this work are Aerosil OX50 (Evonik, Germany).

The "liquid glass" ratio: A homogeneous solution was formed by 29.3 wt % HEMA, 11.5 wt % DEDB, and 4.2 wt % TEGDA. The MYP2011−50 stirrer was used to add 55 wt % OX50 in 10 batches for 20 min at 800 rpm. Following this, 0.5 wt % of Irgacure 819 (photoinitiator) and 0.3 wt % of Sudan Orange G (absorber) were dispersed into the mixture. The mixture was further dispersed, and air bubbles were removed using a vacuum-drying oven.

4.2. Fabrication of Silica-Glass-Based Biomimetic Frame. The printed samples were developed by 5‰ NaOH solution, and the developed samples were subsequently heat treated. The muffle furnace (KSL-1100X, HF-Kejing, China) and the tube furnace (GSL-1500X, HF-Kejing, China) were selected to conduct the debinding and the sintering process, respectively. The debinding process was carried out in an air atmosphere, while the vacuum condition was adopted for sintering.

4.3. Fabrication of Superhydrophobic Nanoparticles. Biomimetic frames were filled with nanoparticles using the in situ deposition method proposed by Deng et al.,[33,41] and Figure 1d,e illustrates the entire process. The frame surface is subjected to a burning candle flame to aggregate carbon nanoparticles onto the microstructure surface. This is followed by chemical vapor deposition (CVD). The surfaces coated with candle soot were exposed to a vacuum environment containing two glass containers, each with 2 mL of TEOS and ammonia, for 24 h at room temperature under vacuum conditions. Silica nanoparticles could be produced by this process. Then, the samples underwent calcination at 600 °C for 2 h to remove the carbon particles and obtain hollow silica nanoparticles. Finally, the composite structure underwent a process of CVD similar to the above steps using FOTS to obtain superhydrophobic properties.

4.4. Characterization. The thermal analyzer (ZCT-A, Beijing JYGK, China) was adopted to obtain the thermogravimetric-differential thermal analysis (TG-DTA) curves of the photopolymerized samples. The composite structure was analyzed using a field emission scanning electron microscope (SEM) (FEI Quanta FEG 250) and an Olympus optical microscope to determine the morphology. The transmittance of the sintered samples was recorded by a Hitachi UH4150 spectrophotometer within the wavelength range of 300 to 900 nm. Structural profiles were obtained by an Alpha-Step D-300 probe profiler. Contact angle testing was completed by KRUSS DSA 100. The experimental errors presented in the graphs were obtained from five independent measurements, and the volume of water droplets used in the manuscript for both static and dynamic contact angle tests was 3 μL.

ASSOCIATED CONTENT

Supporting Information

The Supporting Information is available free of charge at https://pubs.acs.org/doi/10.1021/acsami.3c08125.

Detailed morphology and dynamic and static contact angle test results of allium seeds; extra dynamic and static contact angle tests of BSSG; optical microscope images of BSSG before and after tests; and comparison of performance of superhydrophobic surfaces fabricated by different materials and methods (PDF)

(Movie S1) Self-cleaning performance of BSSG (MOV)

AUTHOR INFORMATION

Corresponding Authors

Zhi Wang − *Changchun Institute of Optics, Fine Mechanics and Physics, Chinese Academy of Sciences, Changchun, Jilin 130033, China*; Email: wangzhi@ciomp.ac.cn

Zhiwei Zhu − *School of Mechanical Engineering, Nanjing University of Science and Technology, Nanjing, J.S 210094, China*; Email: zw.zhu@njust.edu.cn

Hua Liu − *Center for Advanced Optoelectronic Functional Materials Research, and Key Laboratory for UV Emitting Materials and Technology of Ministry of Education, National Demonstration Center for Experimental Physics Education, Northeast Normal University, Changchun, Jilin 130024, China*; orcid.org/0000-0003-1455-8948; Email: liuh146@nenu.edu.cn

Authors

Han Zhang − *Center for Advanced Optoelectronic Functional Materials Research, and Key Laboratory for UV Emitting Materials and Technology of Ministry of Education, National Demonstration Center for Experimental Physics Education, Northeast Normal University, Changchun, Jilin 130024, China*

Yu-Qing Liu − *Center for Advanced Optoelectronic Functional Materials Research, and Key Laboratory for UV Emitting Materials and Technology of Ministry of Education, National Demonstration Center for Experimental Physics Education, Northeast Normal University, Changchun, Jilin 130024, China*

Shaoqing Zhao − *Center for Advanced Optoelectronic Functional Materials Research, and Key Laboratory for UV Emitting Materials and Technology of Ministry of Education, National Demonstration Center for Experimental Physics Education, Northeast Normal University, Changchun, Jilin 130024, China*

Long Huang − *Center for Advanced Optoelectronic Functional Materials Research, and Key Laboratory for UV Emitting Materials and Technology of Ministry of Education, National Demonstration Center for Experimental Physics Education, Northeast Normal University, Changchun, Jilin 130024, China*

Zhiyong Gao − *Changchun Institute of Optics, Fine Mechanics and Physics, Chinese Academy of Sciences, Changchun, Jilin 130033, China*

Dahai Hu − *Center for Advanced Optoelectronic Functional Materials Research, and Key Laboratory for UV Emitting Materials and Technology of Ministry of Education, National Demonstration Center for Experimental Physics Education, Northeast Normal University, Changchun, Jilin 130024, China*

Complete contact information is available at:
https://pubs.acs.org/10.1021/acsami.3c08125

Author Contributions

H.Z. and H.L. conceived, designed, carried out the experiments, and wrote the draft of the manuscript. H.Z., Y.L., H.L., Z.W., and Z.Z. analyzed all the experimental data and reviewed the manuscript. L.H., S.Z., Z.G., and D.H. reviewed and edited the manuscript. All authors contributed to the article and approved the submitted version.

Notes

The authors declare no competing financial interest.

■ ACKNOWLEDGMENTS

This work was supported by the National Natural Science Foundation of China (nos. 62275044, 62205174, and 61875036) and the Jinan "20 New Colleges and Universities" Innovation Team Introduction Project (202228047).

■ REFERENCES

(1) Toombs, J. T.; Luitz, M.; Cook, C. C.; Jenne, S.; Li, C. C.; Rapp, B. E.; Kotz-Helmer, F.; Taylor, H. K. Volumetric additive manufacturing of silica glass with microscale computed axial lithography. *Science* **2022**, *376*, 308−312.
(2) Kotz, F.; Schneider, N.; Striegel, A.; Wolfschläger, A.; Keller, N.; Worgull, M.; Bauer, W.; Schild, D.; Milich, M.; Greiner, C.; Helmer, D.; Rapp, B. E. Glassomer—processing fused silica glass like a polymer. *Adv. Mater.* **2018**, *30*, 1707100.
(3) Zhang, H.; Li, F.; Song, H.; Liu, Y.; Huang, L.; Zhao, S.; Xiong, Z.; Wang, Z.; Dong, Y.; Liu, H. Random Silica-Glass Microlens Arrays Based on the Molding Technology of Photocurable Nanocomposites. *ACS Appl. Mater. Interfaces* **2023**, *15*, 19230−19240.
(4) Zhang, H.; Huang, L.; Tan, M.; Zhao, S.; Liu, H.; Lu, Z.; Li, J.; Liang, Z. Overview of 3d-printed silica glass. *Micromachines* **2022**, *13*, 81.
(5) Sakakura, M.; Lei, Y.; Wang, L.; Yu, Y.-H.; Kazansky, P. G. Ultralow-loss geometric phase and polarization shaping by ultrafast laser writing in silica glass. *Light: Sci. Appl.* **2020**, *9*, 15.
(6) Brückner, R. Properties and structure of vitreous silica. *I. J. Non-Cryst. Solids* **1970**, *5*, 123−175.
(7) Kotz, F.; Arnold, K.; Bauer, W.; Schild, D.; Keller, N.; Sachsenheimer, K.; Nargang, T. M.; Richter, C.; Helmer, D.; Rapp, B. E. Three-dimensional printing of transparent fused silica glass. *Nature* **2017**, *544*, 337−339.
(8) Kotz, F.; Quick, A. S.; Risch, P.; Martin, T.; Hoose, T.; Thiel, M.; Helmer, D.; Rapp, B. E. Two-Photon Polymerization of Nanocomposites for the Fabrication of Transparent Fused Silica Glass Microstructures. *Adv. Mater.* **2021**, *33*, 2006341.
(9) Liu, Y.-Q.; Xiong, Z.; Zhang, Y.-L.; Liu, H. breakthrough of projection-enabled additive manufacturing: from novel strategies to cutting-edge applications. *Innovation* **2023**, *4*, No. 100395.
(10) Moore, D. G.; Barbera, L.; Masania, K.; Studart, A. R. Three-dimensional printing of multicomponent glasses using phase-separating resins. *Nat. Mater.* **2020**, *19*, 212−217.
(11) Doualle, T.; André, J. C.; Gallais, L. 3D printing of silica glass through a multiphoton polymerization process. *Opt. Lett.* **2021**, *46*, 364−367.
(12) Wen, X.; Zhang, B.; Wang, W.; Ye, F.; Yue, S.; Guo, H.; Gao, G.; Zhao, Y.; Fang, Q.; Nguyen, C.; Zhang, X.; Bao, J.; Robinson, J. T.; Ajayan, P. M.; Lou, J. 3D-printed silica with nanoscale resolution. *Nat. Mater.* **2021**, *20*, 1506−1511.
(13) Hong, Z.; Ye, P.; Loy, D. A.; Liang, R. Three-dimensional printing of glass micro-optics. *Optica* **2021**, *8*, 904−910.
(14) Hong, Z.; Ye, P.; Loy, D. A.; Liang, R. High-Precision Printing of Complex Glass Imaging Optics with Precondensed Liquid Silica Resin. *Adv. Sci.* **2022**, *9*, 2105595.
(15) Liu, C.; Oriekhov, T.; Lee, C.; Harvey, C. M.; Fokine, M. Rapid Fabrication of Silica Microlens Arrays via Glass 3D Printing. *3D Print. Addit. Manuf.* **2022**, DOI: 10.1089/3dp.2022.0112.
(16) Gal-Or, E.; Gershoni, Y.; Scotti, G.; Nilsson, S. M. E.; Saarinen, J.; Jokinen, V.; Strachan, C. J.; Boije Af Gennäs, G.; Yli-Kauhaluoma, J.; Kotiaho, T. Chemical analysis using 3D printed glass microfluidics. *Anal. Methods* **2019**, *11*, 1802−1810.
(17) Kotz, F.; Risch, P.; Arnold, K.; Sevim, S.; Puigmartí-Luis, J.; Quick, A.; Thiel, M.; Hrynevich, A.; Dalton, P. D.; Helmer, D.; Rapp, B. E. Fabrication of arbitrary three-dimensional suspended hollow microstructures in transparent fused silica glass. *Nat. Commun.* **2019**, *10*, 1439.
(18) Li, F.; Wang, Z.; Huang, S.; Pan, Y.; Zhao, X. Flexible, Durable, and Unconditioned Superoleophobic/Superhydrophilic Surfaces for Controllable Transport and Oil-Water Separation. *Adv. Funct. Mater.* **2018**, *28*, 1706867.
(19) Yang, P.; Zou, X.; Zhang, Z.; Hong, M.; Shi, J.; Chen, S.; Shu, J.; Zhao, L.; Jiang, S.; Zhou, X.; Huan, Y.; Xie, C.; Gao, P.; Chen, Q.; Zhang, Q.; Liu, Z.; Zhang, Y. Batch production of 6-inch uniform monolayer molybdenum disulfide catalyzed by sodium in glass. *Nat. Commun.* **2018**, *9*, 979.
(20) Wu, Z.; Yan, S.; Ming, T.; Zhao, X.; Zhang, N. Analysis and modeling of dust accumulation-composed spherical and cubic particles on PV module relative transmittance. *Sustainable Energy Technol. Assess.* **2021**, *44*, No. 101015.
(21) Sangpongsanont, Y.; Chenvidhya, D.; Chuangchote, S.; Kirtikara, K. Corrosion growth of solar cells in modules after 15 years of operation. *Sol. Energy* **2020**, *205*, 409−431.
(22) Kim, K.; Park, H. R.; Kim, H. J.; Lee, D.; Ha, S.; Lee, K.; Hwang, W. Self-cleaning mechanisms according to the wettability of the surface and deposition material. *Appl. Surf. Sci.* **2023**, *626*, No. 157197.
(23) Sun, S.; Xu, P.; Chen, Z.-H.; Xiao, Q.-R.; Qiang, X.-L.; Shi, X.-L. "One Stone Three Birds": A multifunctional cotton fabric with favorable self-cleaning, photothermal effect and Joule heating properties. *Appl. Surf. Sci.* **2023**, *623*, 1556961.
(24) Vüllers, F.; Fritz, B.; Roslizar, A.; Striegel, A.; Guttmann, M.; Richards, B. S.; Hölscher, H.; Gomard, G.; Klampaftis, E.; Kavalenka, M. N. Self-Cleaning Microcavity Array for Photovoltaic Modules. *ACS Appl. Mater. Interfaces* **2018**, *10*, 2929−2936.
(25) Selim, M. S.; Yang, H.; Wang, F. Q.; Fatthallah, N. A.; Huang, Y.; Kuga, S. Silicone/ZnO nanorod composite coating as a marine antifouling surface. *Appl. Surf. Sci.* **2019**, *466*, 40−50.
(26) Ensikat, H. J.; Ditsche-Kuru, P.; Neinhuis, C.; Barthlott, W. Superhydrophobicity in perfection: the outstanding properties of the lotus leaf. *Beilstein J. Nanotechnol.* **2011**, *2*, 152−161.
(27) Zhang, W.; Wang, D.; Sun, Z.; Song, J.; Deng, X. Robust superhydrophobicity: mechanisms and strategies. *Chem. Soc. Rev.* **2021**, *50*, 4031−4061.
(28) Yin, K.; Wang, L.; Deng, Q.; Huang, Q.; Jiang, J.; Li, G.; He, J. Femtosecond Laser Thermal Accumulation-Triggered Micro-/Nano-structures with Patternable and Controllable Wettability Towards Liquid Manipulating. *Nano-Micro Lett.* **2022**, *14*, 97.
(29) Chen, Q.; Zhang, C.; Cai, Y.; Luo, X.; Wang, B.; Song, Q.; Liu, Z. Periodically oriented superhydrophobic microstructures prepared by laser ablation-chemical etching process for drag reduction. *Appl. Surf. Sci.* **2023**, *615*, No. 156403.
(30) Li, J.; Zhao, S.; Du, F.; Zhou, Y.; Yu, H. One-step fabrication of superhydrophobic surfaces with different adhesion via laser processing. *J. Alloys Compd.* **2018**, *739*, 489−498.
(31) Xin, G.; Wu, C.; Liu, W.; Rong, Y.; Huang, Y. Anti-corrosion superhydrophobic surfaces of Al alloy based on micro-protrusion array structure fabricated by laser direct writing. *J. Alloys Compd.* **2021**, *881*, No. 160649.
(32) Pan, R.; Zhang, H.; Zhong, M. Triple-scale superhydrophobic surface with excellent anti-icing and icephobic performance via ultrafast laser hybrid fabrication. *ACS Appl. Mater. Interfaces* **2018**, *10*, 2929−2936.

(33) Deng, X.; Mammen, L.; Butt, H. J.; Vollmer, D. Candle soot as a template for a transparent robust superamphiphobic coating. *Science* **2012**, *335*, 67−70.
(34) Luo, W.; Sun, D.; Chen, S.; Shanmugam, L.; Xiang, Y.; Yang, J. Robust microcapsules with durable superhydrophobicity and superoleophilicity for efficient oil−water separation. *ACS Appl. Mater. Interfaces* **2020**, *12*, 57547−57559.
(35) Du, C.; Chen, Y.; He, S.; Ruan, C.; Liu, X.; He, C.; Jin, X.; Chen, Q.; Ma, Y.; Chen, G. Insight into ultra-flexible & robust silica aerogels based on diene synthesis reaction: Preparation and oil/water separation. *Appl. Surf. Sci.* **2022**, *606*, No. 154902.
(36) Zheng, J.; Yang, J.; Cao, W.; Huang, Y.; Zhou, Z.; Huang, Y.-X. Fabrication of transparent wear-resistant superhydrophobic SiO_2 film via phase separation and chemical vapor deposition methods. *Ceram. Int.* **2022**, *48*, 32143−32151.
(37) Huang, X.; Sun, M.; Shi, X.; Shao, J.; Jin, M.; Liu, W.; Zhang, R.; Huang, S.; Ye, Y. Chemical vapor deposition of transparent superhydrophobic anti-Icing coatings with tailored polymer nanoarray architecture. *Chem. Eng. J.* **2023**, *454*, No. 139981.
(38) Luo, H.; Yang, M.; Li, D.; Wang, Q.; Zou, W.; Xu, J.; Zhao, N. Transparent super-repellent surfaces with low haze and high jet impact resistance. *ACS Appl. Mater. Interfaces* **2021**, *13*, 13813−13821.
(39) Zhang, L.-z.; Pan, A.-j.; Cai, R.-r.; Lu, H. Indoor experiments of dust deposition reduction on solar cell covering glass by transparent super-hydrophobic coating with different tilt angles. *Sol. Energy* **2019**, *188*, 1146−1155.
(40) Lyu, J.; Wu, B.; Wu, N.; Peng, C.; Yang, J.; Meng, Y.; Xing, S. Green preparation of transparent superhydrophobic coatings with persistent dynamic impact resistance for outdoor applications. *Chem. Eng. J.* **2021**, *404*, No. 126456.
(41) Wang, D.; Sun, Q.; Hokkanen, M. J.; Zhang, C.; Lin, F.-Y.; Liu, Q.; Zhu, S.-P.; Zhou, T.; Chang, Q.; He, B.; Zhou, Q.; Chen, L.; Wang, Z.; Ras, R. H. A.; Deng, X. Design of robust superhydrophobic surfaces. *Nature* **2020**, *582*, 55−59.
(42) Halloran, J. W. Ceramic Stereolithography: Additive Manufacturing for Ceramics by Photopolymerization. *Annu. Rev. Mater. Res.* **2016**, *46*, 19−40.
(43) Liu, C.; Qian, B.; Liu, X.; Tong, L.; Qiu, J. Additive manufacturing of silica glass using laser stereolithography with a top-down approach and fast debinding. *RSC Adv.* **2018**, *8*, 16344−16348.
(44) Cai, P.; Guo, L.; Wang, H.; Li, J.; Li, J.; Qiu, Y.; Zhang, Q.; Lue, Q. Effects of slurry mixing methods and solid loading on 3D printed silica glass parts based on DLP stereolithography. *Ceram. Int.* **2020**, *46*, 16833−16841.
(45) Zhang, Y.; Dong, Z.; Li, C.; Du, H.; Fang, N. X.; Wu, L.; Song, Y. Continuous 3D printing from one single droplet. *Nat. Commun.* **2020**, *11*, 4685.
(46) Zhang, X.; Pan, Y.; Gao, Q.; Zhao, J.; Wang, Y.; Liu, C.; Shen, C.; Liu, X. Facile fabrication of durable superhydrophobic mesh via candle soot for oil-water separation. *Prog. Org. Coat.* **2019**, *136*, No. 105253.
(47) Domingues, E. M.; Arunachalam, S.; Nauruzbayeva, J.; Mishra, H. Biomimetic coating-free surfaces for long-term entrapment of air under wetting liquids. *Nat. Commun.* **2018**, *9*, 3606.

https://doi.org/10.1021/acsami.3c08125
ACS Appl. Mater. Interfaces 2023, 15, 38132−38142